



HAL
open science

The Extreme Low-mass End of the Mass–Metallicity Relation at $z \sim 7$

Iryna Chemerynska, Hakim Atek, Pratika Dayal, Lukas J. Furtak, Robert Feldmann, Jenny E. Greene, Michael V. Maseda, Themiya Nanayakkara, Pascal A. Oesch, Seiji Fujimoto, et al.

► **To cite this version:**

Iryna Chemerynska, Hakim Atek, Pratika Dayal, Lukas J. Furtak, Robert Feldmann, et al.. The Extreme Low-mass End of the Mass–Metallicity Relation at $z \sim 7$. *The Astrophysical Journal Letters*, 2024, 976, 10.3847/2041-8213/ad8dc9. insu-04851490

HAL Id: insu-04851490

<https://insu.hal.science/insu-04851490v1>

Submitted on 21 Dec 2024

HAL is a multi-disciplinary open access archive for the deposit and dissemination of scientific research documents, whether they are published or not. The documents may come from teaching and research institutions in France or abroad, or from public or private research centers.

L'archive ouverte pluridisciplinaire **HAL**, est destinée au dépôt et à la diffusion de documents scientifiques de niveau recherche, publiés ou non, émanant des établissements d'enseignement et de recherche français ou étrangers, des laboratoires publics ou privés.



Distributed under a Creative Commons Attribution 4.0 International License



The Extreme Low-mass End of the Mass–Metallicity Relation at $z \sim 7$

Iryna Chemerynska¹, Hakim Atek¹, Pratika Dayal², Lukas J. Furtak³, Robert Feldmann⁴, Jenny E. Greene⁵, Michael V. Maseda⁶, Themiya Nanayakkara⁷, Pascal A. Oesch^{8,9}, Seiji Fujimoto^{10,20}, Ivo Labbé¹¹, Rachel Bezanson¹², Gabriel Brammer^{9,13}, Sam E. Cutler¹⁴, Joel Leja^{15,16,17}, Richard Pan¹⁸, Sedona H. Price¹², Bingjie Wang^{15,16,17}, John R. Weaver¹⁴, and Katherine E. Whitaker^{14,19}

¹ Institut d’Astrophysique de Paris, CNRS, Sorbonne Université, 98bis Boulevard Arago, 75014, Paris, France; iryna.chemerynska@iap.fr

² Kapteyn Astronomical Institute, University of Groningen, 9700 AV Groningen, The Netherlands

³ Department of Physics, Ben-Gurion University of the Negev, P.O. Box 653, Be’er-Sheva 84105, Israel

⁴ Department of Astrophysics, University of Zurich, Zurich, CH-8057, Switzerland

⁵ Department of Astrophysical Sciences, Princeton University, 4 Ivy Lane, Princeton, NJ 08544, USA

⁶ Department of Astronomy, University of Wisconsin–Madison, 475 North Charter Street, Madison, WI 53706, USA

⁷ Centre for Astrophysics and Supercomputing, Swinburne University of Technology, PO Box 218, Hawthorn, VIC 3122, Australia

⁸ Department of Astronomy, University of Geneva, Chemin Pegasi 51, 1290 Versoix, Switzerland

⁹ Cosmic Dawn Center (DAWN), Copenhagen, Denmark

¹⁰ Department of Astronomy, The University of Texas at Austin, Austin, TX, USA

¹¹ Centre for Astrophysics and Supercomputing, Swinburne University of Technology, Melbourne, VIC 3122, Australia

¹² Department of Physics and Astronomy and PITT PACC, University of Pittsburgh, Pittsburgh, PA 15260, USA

¹³ Niels Bohr Institute, University of Copenhagen, Jagtvej 128, Copenhagen, Denmark

¹⁴ Department of Astronomy, University of Massachusetts, Amherst, MA 01003, USA

¹⁵ Department of Astronomy & Astrophysics, The Pennsylvania State University, University Park, PA 16802, USA

¹⁶ Institute for Computational & Data Sciences, The Pennsylvania State University, University Park, PA 16802, USA

¹⁷ Institute for Gravitation and the Cosmos, The Pennsylvania State University, University Park, PA 16802, USA

¹⁸ Department of Physics and Astronomy, Tufts University, 574 Boston Avenue, Medford, MA 02155, USA

¹⁹ Cosmic Dawn Center (DAWN), Denmark

Received 2024 July 23; revised 2024 October 23; accepted 2024 October 23; published 2024 November 18

Abstract

The mass–metallicity relation provides crucial insights into the baryon cycle in galaxies and strong constraints on galaxy formation models. We use JWST NIRSpec observations from the UNCOVER program to measure the gas-phase metallicity in a sample of eight galaxies during the epoch of reionization at $z = 6–8$. Thanks to the strong lensing of the galaxy cluster Abell 2744, we are able to probe extremely low stellar masses between 10^6 and $10^8 M_{\odot}$. Using strong-line diagnostics and the most recent JWST calibrations, we derive extremely low oxygen abundances in the range of $12 + \log(\text{O}/\text{H}) = 6.7–7.8$. By combining this sample with more massive galaxies at similar redshifts, we derive a best-fit relation of $12 + \log(\text{O}/\text{H}) = -0.076_{-0.03}^{+0.03} \times (\log(M_{\star}))^2 + 1.61_{-0.52}^{+0.52} \times \log(M_{\star}) - 0.26_{-0.10}^{+0.10}$, which becomes steeper than determinations at $z \sim 3–6$ toward low-mass galaxies. Our results show a clear redshift evolution in the overall normalization of the relation, galaxies at higher redshift having significantly lower metallicities at a given mass. A comparison with theoretical models provides important constraints on which physical processes, such as metal mixing, star formation or feedback recipes, are important in reproducing the observations. Additionally, these galaxies exhibit star formation rates that are higher by a factor of a few to tens compared to extrapolated relations at similar redshifts or theoretical predictions of main-sequence galaxies, pointing to a recent burst of star formation. All these observations are indicative of the highly stochastic star formation and interstellar medium enrichment expected in these low-mass systems, suggesting that feedback mechanisms in high- z dwarf galaxies might be different from those in place at higher masses.

Unified Astronomy Thesaurus concepts: Galaxy formation (595); Galaxy evolution (594); High-redshift galaxies (734); Galaxies (573); Reionization (1383); Gravitational lensing (670); Strong gravitational lensing (1643)

1. Introduction

The chemical composition of the interstellar medium (ISM) is a crucial ingredient in the baryonic cycle within galaxies. A galaxy’s metal content depends on some environmental factors, including the acquisition of metals and gas gained from mergers and through inflows from the intergalactic medium and the loss of metals and gas through outflows. Valuable insights

into galaxy growth can be gained by studying the connection between metallicity (the ratio of metal mass to gas mass) and inherent galaxy properties, such as stellar mass and star formation rate (SFR; R. Maiolino & F. Mannucci 2019). Therefore, metallicity is sensitive to various physical processes that drive the baryon cycle in galaxies.

The gas-phase metallicity in galaxies is often measured through the oxygen abundance, represented as $12 + \log(\text{O}/\text{H})$. The relationship between gas-phase oxygen abundance and stellar mass is known as the mass–metallicity relation (MZR), which is one of the most fundamental scaling relations. It underscores the intricate interplay between star formation, gas inflow and outflow, and the overall chemical evolution of galaxies (C. A. Tremonti et al. 2004; L. J. Kewley & S. L. Ellison 2008). Galaxy metallicity exhibits a tight correlation with stellar mass,

²⁰ Hubble Fellow.

while its scatter is often linked to the SFR (e.g., S. L. Ellison et al. 2008; F. Mannucci et al. 2010) and gas mass (e.g., M. S. Bothwell et al. 2013). As such, it offers crucial insights for theoretical studies of galaxy formation, which need to balance these processes to reproduce the observed properties of galaxies over cosmic history (S. J. Lilly et al. 2013; R. S. Somerville & R. Davé 2015; X. Ma et al. 2016; G. Ucci et al. 2023). Furthermore, it has been suggested that the MZR is a two-dimensional representation of a deeper three-dimensional relationship that connects stellar mass, gas-phase metallicity, and the instantaneous SFR, known as the fundamental metallicity relation (FMR; e.g., S. L. Ellison et al. 2008; P. Dayal et al. 2010; M. A. Lara-López et al. 2010; F. Mannucci et al. 2010; L. Hunt et al. 2012, 2016; M. Curti et al. 2020). However, characterizing these scaling relations at high redshift has been notably restricted to relatively massive galaxies (C. A. Tremonti et al. 2004; A. Henry et al. 2021; R. L. Sanders et al. 2021; K. Nakajima et al. 2023; M. Curti et al. 2024). Consequently, it is unclear whether the MZR extends with the same slope to low-mass galaxies or whether their different star formation histories lead to different baryon cycles and chemical enrichment.

Metallicity measurements ideally require key optical emission lines such as [O III] $\lambda\lambda 5007, 4959$, [O III] $\lambda 4363$, [O II] $\lambda\lambda 3726, 3729$, and the Balmer lines. The JWST can detect auroral lines, such as [O III] $\lambda 4363$, which are generated by collisions between particles at higher energy levels than those typically observed in galaxy spectra. This line is particularly important for gas-phase metallicity studies based on electron temperature (T_e), and the method of determining electron temperatures/metallicities using this line is known as the “direct T_e method” (M. Peimbert 1967; F. Bresolin et al. 2009).

Detecting the auroral line at high redshifts is challenging, so large galaxy samples usually determine metallicities using strong-line diagnostics based on optical nebular lines. These diagnostics are calibrated against metallicities derived using the direct method (M. Curti et al. 2017, 2020; R. L. Sanders et al. 2020; K. Nakajima et al. 2022; I. H. Laseter et al. 2024). Also, the metallicity calibrations are expected to evolve with redshift. There is now substantial evidence suggesting that, at a fixed metallicity, the ionization conditions of the ISM are evolving to a more extreme state at around $z = 2$ (C. C. Steidel et al. 2014; A. E. Shapley et al. 2015; R. L. Sanders et al. 2016, 2020; A. L. Strom et al. 2017). In particular, star-forming galaxies at $z \sim 2-3$ have higher N/O at fixed excitation than $z \sim 0$ galaxies with similar ionizing spectra. This implies the presence of more intense ionizing radiation fields at fixed N/O and O/H levels compared to typical local galaxies. The results of C. C. Steidel et al. (2014) suggest that the systematic offset of high- z galaxies relative to star-forming galaxies in the low-redshift Universe in the N2-BPT ([O III]/ $H\beta$ versus [N II]/ $H\alpha$) plane cautions against using the common strong-line metallicity relations for high-redshift galaxies, since the calibrations are designed to reproduce the local N2-BPT sequence (A. L. Strom et al. 2017). To address this issue, calibrations based on electron temperature T_e were developed using low-redshift galaxies that exhibit extreme line ratios or have similar SFR properties to those of typical high-redshift objects (F. Bian et al. 2018; K. Nakajima et al. 2022). Recent JWST studies have provided important steps toward such calibrations by observing the ratio of [O III] $\lambda 4363$ to the stronger, lower energy level lines of [O III] $\lambda\lambda 4959, 5007$ in $z = 2-8$ galaxies (R. L. Sanders et al. 2024) and $z = 9.5$ (I. H. Laseter et al.

2024). This has allowed particularly for investigation of the MZR at $z > 6$. For example, M. Curti et al. (2023) and K. Nakajima et al. (2023) used a large sample of galaxies from various JWST programs (Early Release Observations (ERO), CEERS, GLASS, JADES) to explore the MZR at these redshifts. Additionally, K. Nakajima et al. (2022), S. Fujimoto et al. (2023), K. E. Heintz et al. (2023), and D. Langeroodi et al. (2023) found that the galaxies at $z > 6$ fall below the MZRs at $z = 0-3$, which may indicate the possible redshift evolution of the MZR. However, all these studies are restricted to relatively massive galaxies and fail to explore the low-mass regime. Extending the MZR to dwarf galaxies ($M_* < 10^8 M_\odot$) provides important leverage for constraining the MZR slope, as the effects of star formation feedback are expected to be more pronounced in these low-mass galaxies due to their weaker gravitational potential (G. Ucci et al. 2023).

Here, we explore for the first time the MZR of extremely low-mass galaxies, down to $M_* \sim 10^6 M_\odot$, during the epoch of reionization. These sources benefit from the strong gravitational magnification of the galaxy cluster Abell 2744 (A2744) and deep NIRSpec spectroscopic observations from the JWST UNCOVER survey (R. Bezanson et al. 2024).

The paper is organized as follows. In Section 2, we describe the imaging data set used in the study, and the lensing model is covered in Section 3. In Section 4, we utilize strong emission line ratios to derive metallicities for the JWST objects with improved NIRSpec spectra. Then we examine the MZR and its correlation with the specific star formation rate (sSFR). In Section 5, we analyze the SFR–mass relations alongside the $SFR_{H\alpha}/SFR_{UV}$ ratio. The implications are discussed in Section 6. The conclusion is given in Section 7.

Throughout this work, we assume a flat Λ CDM cosmology with $H_0 = 70 \text{ km s}^{-1} \text{ Mpc}^{-1}$, $\Omega_M = 0.3$, and $\Omega_\Lambda = 0.7$.

2. Observations

The UNCOVER data set contains multiwavelength NIRCcam imaging of the lensing cluster A2744 in six broadband filters (F115W, F150W, F200W, F277W, F356W, and F444W) and one medium-band filter (F410M) and parallel observations with the Near Infrared Imager and Slitless Spectrograph using five broadband filters (F115W, F150W, F200W, F356W, and F444W). The JWST/NIRSpec low-resolution Prism spectra were collected between 2023 July 31 and August 2 as the second phase of the UNCOVER Treasure survey (PIs: Labbe & Bezanson; JWST-GO-2561; R. Bezanson et al. 2024).

All eight spectroscopic targets were observed with the Micro-Shutter Assembly (MSA), and the MSA observations are separated into seven pointings, with significant overlap in the center, providing total integration times ranging from 2.7 to 17.4 hr. All sources were assigned three slitlets, and observations were conducted with a 2-POINT-WITH-NIRCcam-SIZE2 dither pattern. The data were analyzed using the JWST/NIRSpec analysis software version 0.6.10 `msaexp`. The processing was based on level 2 MAST3 products using the CRDS context file `mwst_1100.pmap`. The software performed various basic reduction steps including flat-field, bias, $1/f$ noise, and snowball correction. It also performed wavelength and photometric calibrations of individual exposure frames (K. E. Heintz et al. 2023).

The photometric component’s observational design is detailed in R. Bezanson et al. (2024), the catalog is explained by J. R. Weaver et al. (2023), and the photometric redshifts are

Table 1
The Photometric and Spectroscopic Characteristics of the Sample of High-redshift Candidates Identified through the A2744 Cluster

ID	M_{UV} AB	z_{spec}	$\log(M_*/M_\odot)$	SFR $_{H\alpha}$ ($M_\odot \text{ yr}^{-1}$)	SFR $_{UV}$ ($M_\odot \text{ yr}^{-1}$)	12+log(O/H)	EW (H β) (\AA)
18924	-15.47 ± 0.08	7.70	$5.88^{+0.13}_{-0.08}$	0.33 ± 0.02	$0.01^{+0.14}_{-0.07}$	6.95 ± 0.15	214.8 ± 39.9
16155	-16.29 ± 0.08	6.87	$6.61^{+0.07}_{-0.06}$	0.92 ± 0.04	$0.04^{+0.08}_{-0.06}$	7.01 ± 0.19	211.9 ± 15.9
23920	-16.18 ± 0.10	6.00	$6.30^{+0.03}_{-0.03}$	1.32 ± 0.04	$0.02^{+0.03}_{-0.03}$	6.84 ± 0.06	334.2 ± 28.2
12899	-15.34 ± 0.11	6.88	$6.54^{+0.14}_{-0.19}$	0.49 ± 0.02	$0.04^{+0.12}_{-0.15}$	6.70 ± 0.15	104.4 ± 31.8
8613	-16.97 ± 0.04	6.38	$7.12^{+0.07}_{-0.08}$	0.78 ± 0.07	$0.16^{+0.08}_{-0.07}$	6.97 ± 0.18	109.0 ± 19.7
23619	-16.55 ± 0.16	6.72	$6.57^{+0.10}_{-0.06}$	0.85 ± 0.07	$0.04^{+0.11}_{-0.05}$	7.19 ± 0.20	35.2 ± 11.7
38335	-16.89 ± 0.13	6.23	$6.83^{+0.25}_{-0.20}$	1.00 ± 0.16	$0.07^{+0.34}_{-0.15}$	7.46 ± 0.32	50.3 ± 35.5
27335	-17.17 ± 0.08	6.75	$6.73^{+0.15}_{-0.08}$	0.73 ± 0.10	$0.05^{+0.17}_{-0.07}$	6.99 ± 0.18	35.7 ± 12.6

Note. More details about the physical properties are given in H. Atek et al. (2024). The oxygen abundance is derived using the calibration of R. L. Sanders et al. (2024).

explored in depth by B. Wang et al. (2023). Refer to S. H. Price et al. (2024) for the spectroscopic experimental design and reductions. The original NIRSPEC sample has been selected in the Hubble Frontier Fields studies of H. Atek et al. (2018) and R. J. Bouwens et al. (2022), based on Hubble Space Telescope observation, in addition to three sources selected from the UNCOVER imaging data based on their photometric redshifts.

3. Gravitational Lensing

In this work, we adopt the $v1.1$ UNCOVER strong-lensing model of A2744, presented in L. J. Furtak et al. (2023b), which is publicly available on the UNCOVER website.²¹ The model is based on the parametric approach by A. Zitrin et al. (2015), which has been updated to be fully analytic and thus not dependent on a fixed grid, which allows for faster computation and with a higher resolution (M. Pascale et al. 2022; L. J. Furtak et al. 2023b). The model for A2744 comprises five smooth cluster-scale dark matter halos, centered on the five brightest cluster galaxies. It consists of 421 cluster member galaxies identified in the $\sim 45 \text{ arcmin}^2$ UNCOVER field of view, as detailed in L. J. Furtak et al. (2023b). The $v1.1$ of the model used here is constrained by a total of 141 multiple images (belonging to 48 sources), of which 96 have spectroscopic redshifts (P. Bergamini et al. 2023a, 2023b; G. Roberts-Borsani et al. 2023) and the remaining ones are photometric systems discovered with the UNCOVER imaging (L. J. Furtak et al. 2023a, 2023b). With these constraints, the model achieves a lens plane image reproduction rms of $\Delta_{rms} = 0''.51$.

4. The MZR

The main goal of the present paper is to investigate the MZR (C. A. Tremonti et al. 2004; F. Mannucci et al. 2010; E. Pérez-Montero et al. 2013; J. H. Lian et al. 2015; R. Maiolino & F. Mannucci 2019; M. Curti et al. 2020; W. M. Baker & R. Maiolino 2023) in extremely low-mass galaxies during the epoch of reionization. The complete process of the sample selection is as follows. Galaxies are drawn from the Hubble Frontier Fields observations of the A2744 cluster. They have been identified as $z > 6$ dropout galaxies using the color-color selection based on the Lyman break technique. This selection was also combined with a photometric redshift estimate that confirmed all these galaxies

to be at $z_{best} > 6$. On top of that, we have selected only galaxies with a high magnification factor, typically higher than $\mu = 2$, to prioritize intrinsically faint galaxies. We ended up with a sample of 14 galaxies. Among these, we were able to fit 10 galaxies in the MSA design. We stress that this selection is solely based on the position of the sources in the sky. Sources were chosen to maximize the total number of sources that can be observed in a single MSA mask. This is because we also had other target categories including active galactic nuclei (AGNs), multiple-image systems, and very high-redshift galaxies. Among these 10 galaxies that were observed with the NIRSPEC MSA, two sources had no usable data (object trace falling in a bad region of the detector or affected by an MSA electrical short). All of the remaining eight sources were spectroscopically confirmed at redshifts between $z = 6$ and $z = 8$. Overall, the only notable selection effect introduced by this procedure is favoring extremely faint galaxies in the rest-frame UV. Therefore, we have selected low-luminosity galaxies that appear to also have very low stellar masses, and we measured their metallicities to probe the extremely low-mass end of the MZR at $z = 6-8$.

The stellar mass of each galaxy is derived from spectral energy distribution (SED) fitting using the `Bagpipes` software (A. C. Carnall et al. 2018, 2019). The procedure simultaneously fits the spectra and the photometric data points. We fit a polynomial function of order 2 to scale the continuum normalization to the photometry. The model library includes G. Bruzual & S. Charlot (2003) stellar population models, the MILES spectral library (P. Sánchez-Blázquez et al. 2006; J. Falcón-Barroso et al. 2011), CLOUDY nebular emission models (G. J. Ferland et al. 2017), and the S. Charlot & S. M. Fall (2000) dust model. We adopt a delayed- τ star formation history (SFR $\propto t^{\tau}$) with the age ($-3 < \log(\text{age}) < 0.48$) and τ ($0.01 < \tau < 5$) as free parameters. By analyzing SED fitting, we identified that the possible stellar population of our galaxies is very young, with stellar ages mostly around a few million years ($t_{50} = 1.08-28.66$). This determination is further supported by the blue UV continuum slopes, which range from $\beta = [-2.07, -2.53]$ and are typically associated with young massive stellar populations and low dust attenuation. A detailed description of the procedure is given in H. Atek et al. (2024). The stellar mass values are shown in Table 1.

Regarding the metallicity measurements, we rely on the strong optical line diagnostics, which have been recently revisited at redshifts greater than $z = 6$ (e.g., K. Nakajima et al.

²¹ <https://jwst-uncover.github.io/DR2.html#LensingMaps>

2023). For our sources, we mainly detect the following rest-frame optical lines ($S/N \gtrsim 2$): $H\alpha + [N II]$, $[O III] \lambda\lambda 4960, 5008, H\beta, H\gamma$, and $[O II] \lambda 3727$. The $[O III] \lambda 4363$ emission is robustly detected in one source only, but it is blended with the $H\delta$ line. Through simultaneous spectral fitting to the continuum and the emission lines, we estimated robust spectroscopic redshifts between $z \sim 6$ and $z \sim 7.70$.

We determine the gas-phase metallicity in our sources by analyzing the strong optical lines. When the auroral lines are not observed, it is possible to use the nebular emission line diagnostics to evaluate the metallicities in the galaxy sample. In the following, we will explore some widely adopted strong-line diagnostics:

$$\begin{aligned} R3 &= \log\left(\frac{[O III] \lambda 5007}{H\beta}\right), \\ R2 &= \log\left(\frac{[O II] \lambda 3727, 3729}{H\beta}\right), \\ O32 &= \log\left(\frac{[O III] \lambda 5007}{[O II] \lambda 3727, 3729}\right). \end{aligned}$$

In order to assess the uncertainties surrounding these indirect diagnostics, we compare different calibrations based on recent JWST observations at high redshift.

4.1. Metallicity Calibrations

In the present study, we adopt two main calibrations published in K. Nakajima et al. (2022) and R. L. Sanders et al. (2024), which are both based on the direct T_e metallicity measurements with the $[O III] \lambda 4363$ line. R. L. Sanders et al. (2024) provided the first high- z strong-line calibrations, which are valid over the low-metallicity range of $12 + \log(O/H) = 7.0$ – 8.4 and can be applied to samples of star-forming galaxies at $z = 2$ – 9 . Regarding the ISM properties, they examine the ionization properties of ~ 160 galaxies at $z = 2$ – 9 from the Cosmic Evolution Early Release Science (CEERS) program (S. L. Finkelstein et al. 2023) by using high-to-low-ionization emission line ratios such as $[O III] \lambda 5007/[O II] \lambda 3727$ and suggest that galaxies tend to present harder ionizing spectra at higher redshift.

Accordingly, I. H. Laseter et al. (2024) compared calibrations for R2, O32, R3, and R23 with their sample and assessed the deviation of each calibration from R. L. Sanders et al. (2024). They found that the R3 and R23 calibrations from R. L. Sanders et al. (2024) do visually trace the upper envelope of their sample, whereas other local calibrations tend to underestimate these ratios. I. H. Laseter et al. (2024) claim that the set of calibrations presented by R. L. Sanders et al. (2024), especially the R3 and R23 diagnostics, are now able to offer a more precise depiction of the distribution of galaxies with direct metallicities in the high- z Universe. It is clear that larger samples of direct metallicity measurements will be needed to obtain a more robust calibration at these redshifts.

We also compare the results with other calibrations derived by K. Nakajima et al. (2022), which are applicable to the low-mass metal-poor galaxies. The metallicities are anchored with the direct method measurements. The gas metallicity diagnostics were established using a combination of local Sloan Digital Sky Survey (SDSS) galaxies and the largest compilation of extremely metal-poor galaxies (XMPGs) identified by the Extremely Metal-poor Representatives Explored by the Subaru Survey (EMPRESS). By using reliable metallicity

measurements from the direct method for low- z galaxies, they derive the relationships between strong optical line ratios and gas-phase metallicity over the range of $12 + \log(O/H) = 6.9$ – 8.9 and explore the mass range of approximately $10^{7.5}$ – $10^{9.5} M_\odot$. In addition to the direct method, they rely on the rest-frame equivalent widths (EWs) of $H\beta$ as an additional parameter to control the ionizing properties of the galaxies. This is because $EW(H\beta)$ is sensitive to the current efficiency of massive star formation and is well correlated with the ionization state as probed by, e.g., O32 (e.g., K. Nakajima & M. Ouchi 2014; M. Mingozi et al. 2020; K. Nakajima et al. 2022).

Additionally, we calculated the metallicities according to a prescription based on the comprehensive emission line catalogs of galaxies from the IllustrisTNG simulation. This includes ionization by stars, AGNs, and shocks to reassess the calibrations of optical metallicity estimators at redshifts $0 < z < 8$ (M. Hirschmann et al. 2023). This calibration was also evaluated against recent JWST results at $4 < z < 9$ (M. Curti et al. 2024; R. L. Sanders et al. 2024). The strong-line diagnostics were estimated on metallicities of $7 \lesssim 12 + \log(O/H) \lesssim 9$ and agreed well with observational results at metallicities below $12 + \log(O/H) \sim 8$.

These additional calibrations and prescriptions are explored in detail in Appendix A. The impact of adopting different calibrations on the MZR relation is also discussed in Appendix B.

4.2. Metallicity Measurements

First, we measure the oxygen abundance using the R3 calibration of R. L. Sanders et al. (2024). For a given value of R3, the calibration defines two metallicity solutions. Although these sources likely have low metallicities, we use the O32 ratio to distinguish between the two branches. For most of the sources, the $[O II]$ is not detected, which provides a lower limit on O32, which is found to vary in the range $O32 = [0.5$ – $1.8]$. Using the O32 metallicity indicator, the resulting values are all compatible with the low-metallicity branch solution. The metallicity measurements are reported in Table 1.

With the goal of exploring systematic differences between metallicity calibrations at high redshift, we also used K. Nakajima et al. (2022) strong-line calibration prescriptions. In addition to the R3–metallicity relation, we attempt to account for the ionization parameter using the $H\beta$ EW (large $EW > 200 \text{ \AA}$, small $EW < 200 \text{ \AA}$). For $[O III] \lambda 4363$ emitters, the rest-frame EWs($H\beta$) can range between 10 and 600 \AA (e.g., R. Maiolino & F. Mannucci 2019; Y. I. Izotov et al. 2021; I. H. Laseter et al. 2022; K. Nakajima et al. 2022). The fit from K. Nakajima et al. (2022) for the large EW is based on the most extreme EW($H\beta$) objects in their calibration sample. We found that the median value of $EW(H\beta)$ for our sample is 136 \AA , with a minimum value of $\sim 35 \text{ \AA}$ and the maximum being $\sim 334 \text{ \AA}$ (see Table 1).

Furthermore, we also used the calibration proposed by I. H. Laseter et al. (2024; JADES) to test the results obtained from the calibrations mentioned above. For this purpose, we employed an alternative diagnostic based on a different combination of R3 and R2 with a higher dynamic range, defined as $\hat{R} = 0.47 \times R2 + 0.88 \times R3$. As mentioned earlier, the $[O II]$ line is not detected for the majority of the sources. Thus, we calculated the upper limits of \hat{R} . The obtained values are found to lie between the results from the

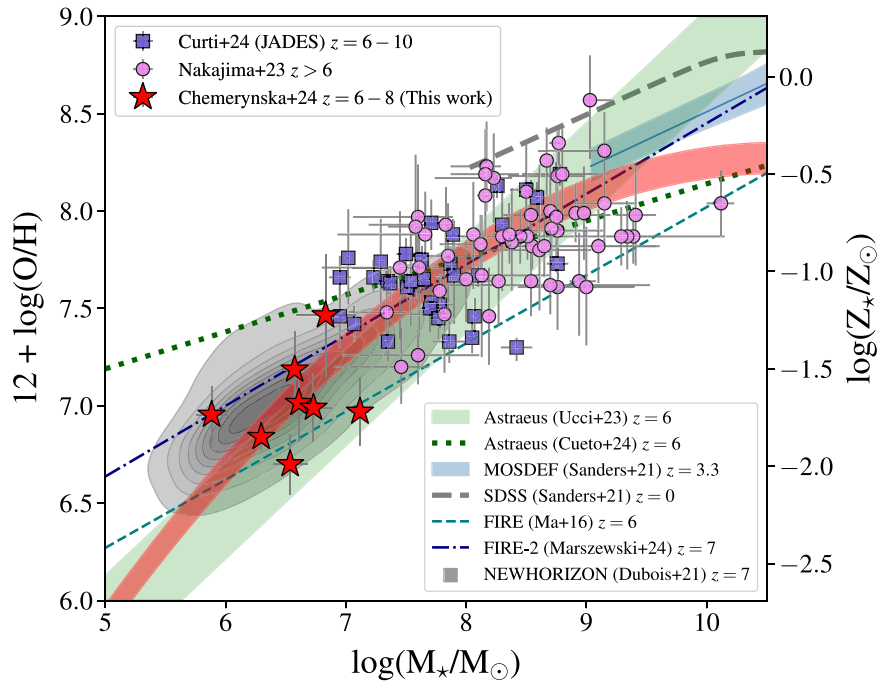


Figure 1. Extending the MZR at $z=6-8$ to the lowest-mass galaxies. The red stars represent measurements of the present sample (the best-fit relation is the red shaded region) based on R. L. Sanders et al. (2024) calibration compared to literature results at similar redshifts: the JADES survey (M. Curti et al. 2024; blue squares) and JWST public surveys (K. Nakajima et al. 2023; violet circles). We also show for reference a lower-redshift determination at $z=0$ from the SDSS (R. L. Sanders et al. 2021; gray dashed line) and at $z=3.3$ from MOSDEF (R. L. Sanders et al. 2021; blue shaded region and line). A comparison to theoretical predictions of the MZR is also provided: the FIRE simulations over the redshift range $z=6$ (X. Ma et al. 2016; teal dashed line), the FIRE-2 simulations at redshift 7 (A. Marszewski et al. 2024; purple dotted-dashed line), the ASTRAEUS determination at $z=6$ (G. Ucci et al. 2023; green shaded region) assuming $\text{SFR} = [0.1-0.5] M_{\odot} \text{ yr}^{-1}$, ASTRAEUS at $z=6$ assuming an evolving IMF (E. R. Cueto et al. 2024; green dotted line), and the NEWHORIZON simulation at the redshift $z=7$ (Y. Dubois et al. 2021; gray shaded region).

K. Nakajima et al. (2022), M. Hirschmann et al. (2023), and R. L. Sanders et al. (2024) calibrations.

With all calibrations, we find extremely low metallicities, in the range of $12 + \log(\text{O}/\text{H}) = 6.70-7.76$, which corresponds to 1%–6% of the solar metallicity. Such low metallicities often suggest that there is likely strong ionizing radiation from massive stars. Due to their pristine gas conditions, these distant low-mass galaxies are expected to be metal-poor. Another possible reason is that there was not enough time for the pre-enrichment, and many metals were lost due to the outflows.

Comparing these results to the low-redshift galaxies, XMPGs can show similar properties and comparable metallicities. For example, EMPRESS has explored the MZR for XMPGs in the local Universe (T. Kojima et al. 2020). Their sample probes a low stellar mass regime ($\log(M_{*}/M_{\odot}) = 5-7$). However, at a fixed stellar mass, their metallicities ($12 + \log(\text{O}/\text{H}) = 6.9-8.5$) span a larger range compared to the present study. Only two of their extreme galaxies show similar metallicities. Uncertainties in our metallicity measurements can explain part of these differences. For instance, the calibration of K. Nakajima et al. (2022) produces slightly higher metallicities, which are more in line with the XMPG values (see Appendix B). On the other hand, we note that our sample was essentially selected based on the UV luminosity (see Section 4), whereas the XMPG sample selection was specifically designed to identify low-metallicity galaxies.

In the recent study of XMPGs in the Dark Energy Spectroscopic Instrument Early Data, H. Zou et al. (2024) analyzed a large sample of galaxies at $z < 1$, for which metallicities are measured using the direct method. Again, while a significant number of their galaxies are located below

the local MZR for normal galaxies, they still have higher metallicities than our galaxies. Overall, given the different selection methods, our galaxies generally show metallicities comparable to XMPGs in the local Universe, and even to a few extreme cases, which may be the only sources that may serve as local analogs of high-redshift low-mass galaxies.

4.3. Extending the MZR to Low-mass Galaxies at $z \sim 7$

We measured the gas-phase metallicity using the $R3 = [\text{O III}]/\text{H}\beta$ line ratio based on the most recent calibrations (K. Nakajima et al. 2022; R. L. Sanders et al. 2024). In Figure 1, we report the oxygen abundance in units of $12 + \log(\text{O}/\text{H})$ as a function of the stellar mass, MZR, and literature results for more massive galaxies. These measurements are based on the R. L. Sanders et al. (2024) calibration. We included results of more massive galaxies from K. Nakajima et al. (2023) and M. Curti et al. (2024) at $z > 6$.

M. Curti et al. (2024) analyzed the gas-phase metallicity properties of a sample of low stellar mass ($\log(M_{*}/M_{\odot}) \lesssim 9$) galaxies at $3 < z < 10$ observed with JWST/NIRSpec as part of the JADES program. In order to extend the parameter space, they complement their sample with a sample of ~ 80 high stellar mass galaxies at the same redshift from other programs (K. Nakajima et al. 2023, CEERS; M. Curti et al. 2023, ERO; A. J. Bunker et al. 2023, GN-z11). In total, the sample consists of 146 galaxies, for which the scaling relations between stellar mass, oxygen abundance, and SFR were explored. The coverage of the low end of the stellar mass distribution is $M_{*}/M_{\odot} \approx 10^{6.5}-10^{10}$. In K. Nakajima et al. (2023), they identified 135 galaxies at $z=4-10$ observed by JWST/NIRSpec. They divided their full sample of ERO, GLASS,

and CEERS galaxies into three subsamples at different redshift bins: $z = 4\text{--}6$, $6\text{--}8$, and $8\text{--}10$. In each panel, the subsample is further divided into two groups based on their masses and average values. Both studies derived metallicities using calibration based on the local metal-poor galaxies (M. Curti et al. 2020; K. Nakajima et al. 2022).

Most theoretical studies predict MZR as a power law (e.g., P. Torrey et al. 2019). Analyzing the MZR, derived from observations, over a wide mass range also shows that it is well fitted with higher-order polynomials (C. A. Tremonti et al. 2004; L. J. Kewley & S. L. Ellison 2008; H. J. Zahid et al. 2014; M. Curti et al. 2020). However, in the mass regime lower than $10^{10} M_{\odot}$, many studies adopt a single power law (H. Lee et al. 2006; R. L. Sanders et al. 2021; K. Nakajima et al. 2022), as the correlation is roughly linear between $10^{8.5}$ and $10^{10.5} M_{\odot}$, and flattening at higher masses. For the first time, we extended the MZR to an extremely low-mass regime. In order to provide a comprehensive picture and account for the possibility of a more complex MZR, we explored a second-order relation fit. We also included the single power-law fit in Appendix B. The second-order fit results in a slightly better $\chi^2 = 1.35$ compared to the single power law ($\chi^2 = 1.40$). The best-fit relation is given by

$$12 + \log(\text{O}/\text{H}) = -0.076_{-0.03}^{+0.03} \times (\log(M_{\star}))^2 \\ + 1.61_{-0.52}^{+0.52} \times \log(M_{\star}) - 0.26_{-0.10}^{+0.10}$$

and is shown with a red shaded region, which represents the $1 - \sigma$ uncertainties of the fit. Compared to an extrapolation of $z = 0$ MZR, these high-redshift galaxies clearly present much lower metallicities at a fixed mass, which reflects the redshift evolution of the MZR and, in turn, the SFR evolution, also called the FMR. Recent studies have observed the same trend, where high- z galaxies exhibit lower metallicities than local analogs with equivalent stellar masses of $M_{\star}/M_{\odot} = 10^{7.5}\text{--}10^{10}$, predicting the relative evolution of the MZR with redshift (K. E. Heintz et al. 2023; D. Langeroodi et al. 2023). A comparison to simulations shows that the derived relation matches the seminumerical rAdiative tranSfer coupling of galaxy formaTion and Reionization in N -body dark matter simUlationS (ASTRAEUS) predictions at $z = 6$ (G. Ucci et al. 2023) and is steeper than the updated ASTRAEUS at the low-mass regime, which includes an evolving initial mass function (IMF) with redshift and depends on the metallicity of the star-forming gas (E. R. Cueto et al. 2024). Here we plot the extrapolated relation to lower masses, as the simulation does not go below $10^7 M_{\odot}$. Our results are slightly steeper than the Feedback In Realistic Environment (FIRE) simulations (X. Ma et al. 2016). Our results appear to lie between FIRE and the recent results of FIRE-2 simulations (A. Marszewski et al. 2024), which have provided high-quality ISM metallicity prescriptions and enabled the characterization of the MZR. Similarly, our results are in line with the NEWHORIZON simulations (Y. Dubois et al. 2021) at similar redshifts. The most recent simulations seem to better reproduce the metal content of the lowest-mass galaxies. They track metal enrichment through the stellar winds, Type II supernova (SN) and Type Ia SN explosions, and asymptotic giant branch stars.

A comparison to results at lower redshifts shows a redshift evolution in the overall normalization of the MZR. At a given

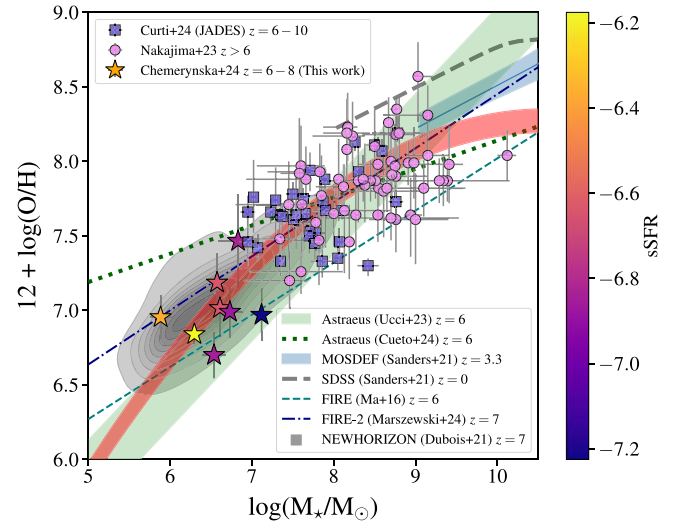


Figure 2. The impact of SFR on the MZR. The stars represent measurements of the present sample, which are color-coded according to their sSFR. The rest of the legend is identical to Figure 1.

stellar mass, galaxies at higher redshifts have lower metallicities. Specifically, local galaxies (SDSS) exhibit metallicities approximately 0.5 dex higher than high-redshift galaxies.

We note that our metallicity estimates are based on the calibration of strong-line diagnostics. These diagnostics depend on the ionization parameter (e.g., L. S. Pilyugin & E. K. Grebel 2016). Therefore, we expect that any variation in this parameter may introduce variability in the inferred metallicity.

We have also explored the effect of adopting different high- z metallicity calibrations on the MZR best-fit relation. The results based on the prescriptions of K. Nakajima et al. (2022) or I. H. Laseter et al. (2024) are shown in Appendix B. To guide the eye, we also plot a single power-law best-fit relation to the data (using binned data from the literature) to highlight how the metallicity data points move upward and downward.

In addition to the mass–metallicity correlation, a second dependency is observed with the SFR. This redshift-invariant FMR can describe the general evolution of the MZR and the SFR correlation. Such a dependence was observed in both observational results (F. Mannucci et al. 2010) and simulations (A. M. Garcia et al. 2024). In Figure 2, we color-coded our sample by sSFR to identify the secondary dependence. Our galaxies tend to have a higher sSFR than the main sequence of galaxies. As discussed by I. H. Laseter et al. (2024), it is expected that with decreasing metallicities and/or masses, there will be an increase in sSFR. This relationship with sSFR at $z > 5$ was also reported in simulations (G. Ucci et al. 2023). However, recent JWST observations have challenged this picture at high redshift, showing deviations from the FMR at $z > 3$ (e.g., M. Curti et al. 2023; K. E. Heintz et al. 2023; T. Morishita et al. 2024). In this study, we find weak evidence for the existence of the FMR at $z \sim 7$.

5. The SFR– M_{\star} Relation

A strong correlation between the SFR and the stellar mass of star-forming galaxies has been established across a wide range of redshifts (J. Brinchmann et al. 2004; K. G. Noeske et al. 2007; K. E. Whitaker et al. 2014; H. Atek et al. 2022). The so-called star-forming “main sequence” (SFMS) reflects the steady stellar mass buildup in galaxies over hundreds of Myr. The

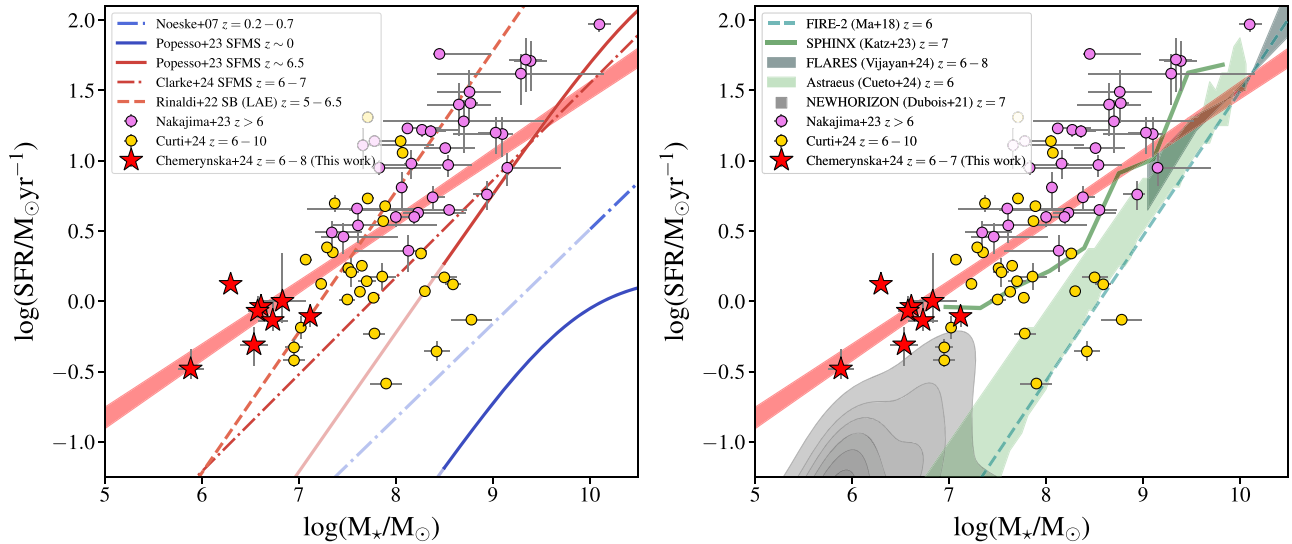


Figure 3. The relationship between stellar mass (M_*) and SFR for our JWST sample (red stars), including the literature sample compiled from K. Nakajima et al. (2023; violet dots; CEERS) and M. Curti et al. (2024; gold dots; EROs). Left: comparison between our best-fit galaxy and the main sequence of star-forming galaxies determined from the literature at $z \sim 0$ and $z \sim 6.5$ (P. Popesso et al. 2023; solid blue and dark red lines, respectively), at $6 < z \lesssim 7$ (L. Clarke et al. 2024; dotted-dashed dark red line), at $0.2 < z < 0.7$ (K. G. Noeske et al. 2007; dotted-dashed blue line), and a starburst cloud at high redshift (P. Rinaldi et al. 2022; dashed red line). The extrapolation for lower masses is depicted in lighter shades. Literature results are color-coded depending on the redshift. Right: we also provided recent results from the SPHINX simulation for SFMS for 10 Myr at $z = 7$ (H. Katz et al. 2023; green solid line), the FLARES simulation at $z = 6-8$ (A. P. Vijayan et al. 2024; gray shaded region) with SFR timescale 100 Myr, ASTRAEUS at $z = 6$ with an evolving IMF (E. R. Cueto et al. 2024; green shaded region), the FIRE-2 simulations at redshift $z = 6$ with SFR averaged over 10 Myr (X. Ma et al. 2018; teal dashed line), and the NEWHORIZON simulation for SFR for 10 Myr at the same redshift (Y. Dubois et al. 2021; gray shaded region). The red shaded area in both figures indicates uncertainties in the fitting.

slope and dispersion of the relation are good indicators of the star formation histories in a given population of galaxies. Reproducing the SFR– M_* relation is also an important requirement for galaxy formation models (e.g., M. Sparre et al. 2015; H. Katz et al. 2023). The advent of JWST has also allowed us to investigate the existence of this relation out to the highest redshifts (L. Clarke et al. 2024). The present sample extends the high-redshift constraints on the SFMS to extremely low-mass galaxies, allowing us to determine whether dwarf galaxies at $z = 6-8$ follow the same star formation history as their massive counterparts.

In Figure 3, we plot the correlation between the SFR and M_* for our sample of galaxies (red stars). We compute the SFR using the $H\alpha$ recombination line, while the stellar mass is derived from SED fitting (see Section 4). We compare our results to the most recent measurements based on JWST observations at similar redshifts (P. Rinaldi et al. 2022; K. Nakajima et al. 2023; L. Clarke et al. 2024; M. Curti et al. 2024). Combining our sample with the literature results of K. Nakajima et al. (2023) and M. Curti et al. (2024), which probe higher stellar masses, we derive the following best-fit relation between the SFR and stellar mass:

$$\log(\text{SFR}) = 0.47^{+0.06}_{-0.06} \times \log(M_*) - 3.17^{+0.12}_{-0.12}.$$

For comparison, we also plot the low-redshift parameterization of the SFMS (K. G. Noeske et al. 2007), the literature compilation of P. Popesso et al. (2023) at both $z = 0$ and $z = 6.5$, and, finally, the relation derived for starburst galaxies by P. Rinaldi et al. (2022) at redshifts 5–6.5. The most striking result is the significant offset of this low-mass sample from the literature results and their respective extrapolation to lower masses. At a given stellar mass, the galaxies in the present sample show higher SFRs by a factor ranging from a few to tens compared to SFR– M_* relations at similar redshifts. Our sample is located even above the starburst sample of P. Rinaldi et al.

(2022). Perhaps this is not surprising since their sample consists of Ly α emitters for which the SFR is derived from their SED fitting or UV luminosity, which traces star formation on different timescales. Additionally, P. Rinaldi et al. (2024) demonstrate that for $\log(M_*/M_\odot) < 7$, there is no clear distinction between main-sequence and starburst galaxies. This trend could be explained by an increased burstiness of star formation, which becomes more significant as stellar mass decreases, or by the limitations of current observational depth. When comparing different samples, the same caveat applies to the compilation of P. Popesso et al. (2023), where galaxies at high redshift lack hydrogen recombination lines for their SFR estimates. The notable exceptions here are the samples of K. Nakajima et al. (2023) and M. Curti et al. (2024), for which the SFRs are measured from either $H\alpha$ or $H\beta$ emission lines and the stellar mass was derived with BEAGLE and PROSPECTOR, respectively. This is precisely why these samples are included in our fitting of the SFR– M_* relation described above. Besides the offset that may indicate a flattening of this relation at lower masses, the best-fit relation shows a shallower slope than the high-redshift determinations. Because we might expect such an offset in galaxies selected by their strong emission lines, it is worth noting that the selection of this sample was only based on the faint UV luminosity (and/or high lensing amplification factors). Therefore, this is clearly an indication of a recent burst of star formation, which is better captured by the $H\alpha$ emission that responds to short-lived massive stars over a few Myr. When comparing the SFR indicators based on $H\alpha$ and UV, we observed values ranging between $\text{SFR}_{H\alpha}/\text{SFR}_{UV} \sim 5$ and $\text{SFR}_{H\alpha}/\text{SFR}_{UV} \sim 66$. While this might well indicate burst-dominated star formation in low-mass galaxies at early times, a larger sample of dwarf galaxies, with stellar masses around $10^6 M_\odot$, is needed to confirm this trend. A statistical sample will also help characterize the duty cycle of this stochastic star formation history.

6. Comparison with Theoretical Models

Our observed sources have stellar masses ranging between $10^{5.9}$ and $10^{7.1} M_{\odot}$ with metallicities in the range of $12 + \log(\text{O}/\text{H}) = 6.8\text{--}7.8$. We now compare these physical properties to the predictions of different theoretical models of galaxy formation. We first consider ASTRAEUS (A. Hutter et al. 2021; G. Ucci et al. 2023), a seminumerical model coupling galaxy formation and reionization on 230 Mpc scales that simulates the MZR between $\sim 10^{6.5\text{--}10} M_{\odot}$ in stellar mass tuned against $z \sim 5\text{--}10$ observables. The second set of predictions is from the FIRE (X. Ma et al. 2016) zoom-in simulations that can track the MZR in the range of $\sim 10^{3\text{--}9} M_{\odot}$ in stellar mass, which are calibrated against $z \sim 0\text{--}3$ data. We also explore the most recent FIRE-2 suite of simulations (X. Ma et al. 2018), tuned for the $z > 5$ Universe. Finally, we also plot the MZR for simulated galaxies at $z = 6$ from NEWHORIZON (Y. Dubois et al. 2021), which combines an intermediate volume (16 Mpc)³ and a high resolution (34 pc) in order to capture the multiphase structure of the ISM.

From our metallicity measurements, the bulk of the observed galaxies overlap with the predictions of ASTRAEUS. ASTRAEUS simulations assume that low-mass galaxies form stars at the maximum limit (at which SN energy balances the halo binding energy) and that there is perfect, instantaneous metal mixing in the ISM. It incorporates key processes of gas accretion, cooling, star formation, and feedback from SNe and AGNs. The model does not show a significant effect of reionization feedback at these redshifts. In Figure 2, we explored the potential impact of sSFR on the MZR, which is directly related to the FMR. However, with a limited sample size, it is challenging to derive a statistically meaningful three-parameter relation. Furthermore, we explore the recent implementation of the evolving IMF into ASTRAEUS (E. R. Cueto et al. 2024). The IMF evolves in each galaxy according to the metallicity of its star-forming gas and redshift. It includes dependence on the SN feedback, metal enrichment, and both ionizing and UV radiation. The amount of newly formed metals depends on the quantity of massive stars that explode as SNe during the current time step. The simulation is limited to a mass range above $10^7 M_{\odot}$. Our findings are located below the extrapolation of this simulation. These findings suggest that, in general, ASTRAEUS conforms to a broad range of the MZR relation, where significant variations can be observed at lower masses depending on the adopted model.

The FIRE simulations use a density threshold for star formation at $10\text{--}100 \text{ cm}^{-3}$ and allow imperfect mixing of metals in the ISM. On the other hand, the new suite of FIRE-2 simulations uses a density threshold of 1000 cm^{-3} to trigger star formation. This new version tracks the abundances of several metals, which are injected in the ISM via SN feedback and stellar winds. In addition, the simulations incorporate subgrid turbulent processes to allow for efficient metal mixing. FIRE-2 simulations predict metallicities 0.3–0.4 dex higher than FIRE. The best-fit MZR relations predicted by the two simulations bracket our measurements around $z = 7$.

The NEWHORIZON cosmological simulations are designed to capture the multiscale ISM physics in an average-density environment. It includes star formation above a density threshold of 10 cm^{-3} with varying efficiency, which evolves with time to become more bursty at high redshift, as well as feedback from SNe and massive stars. It assumes that an SN

explodes when a star particle becomes older than 5 Myr. Although their statistics are more suited for intermediate-mass galaxies, they also cover the physical properties of galaxies down to $\sim 10^6 M_{\odot}$. Because the simulations do not track the evolution of individual elements, the oxygen abundance is scaled assuming a solar metallicity. Despite these crude prescriptions, the predictions align remarkably well with our observations.

Overall, these low-mass galaxies exhibit low gas-phase metallicities, most likely due to low SFRs, which lead to the production of fewer metals in combination with a dilution effect due to gas accretion. In addition, a large fraction of the metals are easily lost due to their shallow potential that enables strong outflows. Theoretical models (e.g., G. Ucci et al. 2023) have shown that the gas mass lost in outflows is higher in low-mass galaxies. If these processes happen on short timescales, then we expect a larger scatter in the MZR at lower masses. It must be noted that none of these models have been tuned to reproduce the unprecedented data presented here for dwarf galaxies at $z \sim 7$. It is therefore heartening to see the reasonable agreement with the data despite their different formalisms for star formation, feedback, and metal enrichment. Our observations therefore present a crucial resource to baseline theoretical models.

7. Summary

Combining the strong gravitational lensing of A2744 and ultra-deep NIRSPEC observations, we were able for the first time to extend the MZR to extremely low-mass galaxies during the epoch of reionization ($6 < z < 8$). Our sample consists of eight galaxies with intrinsic magnitudes in the range $-17.17 < M_{\text{UV}} < -15.47$. Using SED fitting of the spectrophotometric data, we derived low stellar masses down to $\sim 10^6 M_{\odot}$, corrected for amplification. We measured gas-phase metallicities using strong-line diagnostics together with the most recent JWST calibrations (R. L. Sanders et al. 2024). Our measurements yield very low oxygen abundances, in the range $12 + \log(\text{O}/\text{H}) = 6.70\text{--}7.76$, corresponding to 1%–6% of the solar metallicity.

The central goal of the present study is to explore how the MZR in low-mass galaxies compares to their massive counterparts in terms of the slope and normalization. We find a clear offset in the overall normalization of the MZR compared to extrapolations of local or $z = 3$ relations based on more massive galaxies, indicating a strong redshift evolution.

Along these lines, we also investigated the SFR and stellar mass relation, called the star formation main sequence. At a given stellar mass, the galaxies in our sample exhibit a higher SFR by a factor ranging from a few to tens compared to samples at similar redshifts. This suggests a recent burst of star formation, which reflects short-lived massive stars over a few million years. We also find evidence for bursty star formation by analyzing their $\text{SFR}_{\text{H}\alpha}/\text{SFR}_{\text{UV}}$ ratio. However, a larger sample of dwarf galaxies with stellar masses around $10^6 M_{\odot}$ is needed to confirm this trend and characterize the parameters of this stochastic star formation history.

A comparison to galaxy formation models indicates an overall agreement with NEWHORIZON simulations. The FIRE and FIRE-2 suites of simulations, which differ in the implementation of several physical processes, including the metal mixing efficiency, encompass most of our measurements and show a coarse agreement with the slope of the MZR. The

median MZR predictions of the ASTRAEUS set of simulations, which show a broad range of metallicities based on different models, encompass the observational constraints of the present sample.

Overall, these low-mass galaxies exhibit low gas-phase metallicities, likely due to low SFRs that produce fewer metals and potentially episodes of gas accretion. Additionally, a significant fraction of the metals are easily ejected due to strong outflows in low-mass galaxies. The reasonable agreement between our data and theoretical models, despite different formalisms for star formation, feedback, and metal enrichment, is encouraging. Our observations thus provide a crucial resource for benchmarking theoretical models.

Acknowledgments

This work is based on observations obtained with the NASA/ESA/CSA JWST and the NASA/ESA Hubble Space Telescope (HST), retrieved from the Mikulski Archive for Space Telescopes (MAST) at the Space Telescope Science Institute (STScI). STScI is operated by the Association of Universities for Research in Astronomy, Inc., under NASA contract NAS 5-26555. This work has made use of the CANDIDE Cluster at the Institut d’Astrophysique de Paris (IAP), made possible by grants from the PNCG and the region of Île de France through the program DIM-ACAV+. This work was supported by CNES, focused on the JWST mission. This work was supported by the Program National Cosmology and Galaxies (PNCG) of CNRS/INSU with INP and IN2P3, cofunded by CEA and CNES. I.C. acknowledges funding support from the Initiative Physique des Infinis (IPI), a research training program of the Idex SUPER at Sorbonne Université. P.D. acknowledges support from the NWO grant 016.VIDI.189.162 (“ODIN”) and warmly thanks the European Commission’s and University of Groningen’s CO-FUND Rosalind Franklin program.

Data Availability

The data underlying this article are publicly available on the Mikulski Archive for Space Telescopes (MAST)²² under program ID 2561. The specific observations analyzed can be

accessed via doi:[10.17909/c9cj-cd41](https://doi.org/10.17909/c9cj-cd41). Reduced and calibrated mosaics are also available on the UNCOVER webpage.²³

Appendix A Strong-line Diagnostics

In Section 4, we described the high-redshift calibration used in this study. We compared two recent calibrations (K. Nakajima et al. 2022; R. L. Sanders et al. 2024) and simulation results (M. Hirschmann et al. 2023) to derive the metallicity of $z = 6-8$ galaxies. From those calibrations, we adopted the best fit of the R3 diagnostic (see the left panel of Figure 4). For K. Nakajima et al. (2022), we also took into account the dependence on the $EW(H\beta)$ as it was described in the study (a blue curve for the “All” sample and a green curve for the sample with $EW > 200 \text{ \AA}$). We see that for a fixed value of R3, we obtained different values of metallicity. We adopted the R. L. Sanders et al. (2024) calibration as our fiducial metallicity estimator, since the rest of the studies rely on a set of locally calibrated strong-line diagnostics, which may overestimate the metallicities. Additionally, we noticed that metallicities predicted with the simulation IllustrisTNG (M. Hirschmann et al. 2023) also indicate lower metallicities at high redshifts, which is consistent with the calibration derived by R. L. Sanders et al. (2024). In order to confirm the metallicities we derived with the R3 diagnostic, we also probe \hat{R} , which is a novel calibration derived by I. H. Laseter et al. (2024) and was earlier introduced by R. Maiolino et al. (2008) and M. Curti et al. (2017). It is a combination of R2 and R3 in the form

$$\hat{R} = \cos(\phi)R2 + \sin(\phi)R3,$$

which is equivalent to a rotation of the R2–R3 plane around the O/H axis. They used the fourth-order polynomial to the resulting \hat{R} ratio versus the metallicity in the form of $\hat{R} = \sum_n c_n \cdot x^n$, where $x = 12 + \log(O/H) - 8.69$, and identified the angle ϕ that allows the scatter to be minimized in metallicity from the best-fit relation. In this fit, $\phi = 61.^\circ 82$, which translates into $\hat{R} = 0.47R2 + 0.88R3$.

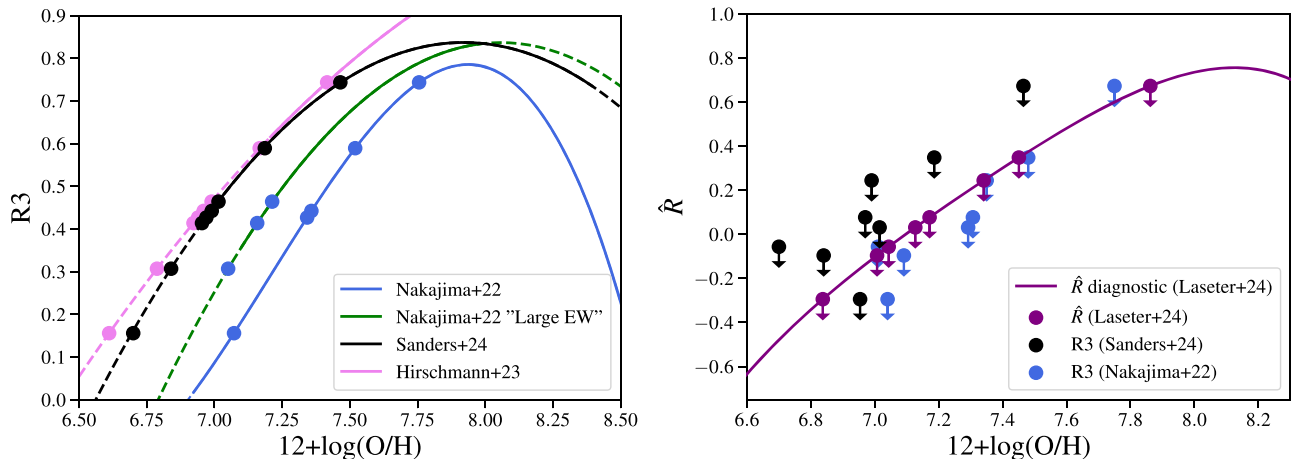


Figure 4. Relationships between metallicity and the strong line ratios of R3 and \hat{R} (from left to right).

²² <https://archive.stsci.edu/>

²³ <https://jwst-uncover.github.io/>

Table 2

Comparison between Oxygen Abundances, $12 + \log(\text{O}/\text{H})$, Derived Using Recent High- z Calibrations or Locally Calibrated Strong-line Diagnostics

ID	I. H. Laseter et al. (2024)	K. Nakajima et al. (2022)	M. Hirschmann et al. (2023)
18924	6.84 ± 0.15	7.16 ± 0.15	6.92 ± 0.15
16155	7.13 ± 0.19	7.21 ± 0.19	6.99 ± 0.19
23920	7.01 ± 0.06	7.05 ± 0.06	6.79 ± 0.06
12899	7.04 ± 0.15	7.07 ± 0.15	6.61 ± 0.15
8613	7.17 ± 0.18	7.34 ± 0.18	6.94 ± 0.18
23619	7.45 ± 0.2	7.52 ± 0.2	7.17 ± 0.2
38355	7.86 ± 0.32	7.76 ± 0.32	7.42 ± 0.32
27335	7.34 ± 0.18	7.36 ± 0.18	6.96 ± 0.18

As mentioned in Section 4, we did not detect the [O II] line for the majority of our sample, but we were able to derive the upper limits on R2 and thus on \hat{R} . In Figure 4 (right panel), we compared the metallicities we obtained using different calibrations. For K. Nakajima et al. (2022) and R. L. Sanders et al. (2024), we calculated metallicities using the R3 diagnostic and then estimated \hat{R} by using the I. H. Laseter et al. (2024) fit mentioned above. As \hat{R} provides us with upper limits, it means that true metallicities will have lower values. The metallicities derived from the different calibrations are presented in Table 2.

Appendix B Comparison of High- z Metallicity Calibrations

In Section 4, we covered the MZR for a combined sample of observed galaxies with the JWST. Here we also estimate the MZR by using additional high- z calibrations to see to what extent our results are affected. We used the simple fit relation in the form

$$12 + \log(\text{O}/\text{H}) = m \times \log(M_*) + b.$$

In Figure 5, we display in each panel the resulting MZR for a given calibration (pink stars) compared to the fiducial calibration (red stars). The top left panel shows the MZR with adopting a single power law using the R. L. Sanders et al. (2024) calibration, $m = 0.39_{-0.02}^{+0.02}$, $b = 4.52_{-0.17}^{+0.17}$. The slope of the relation is shallower, with $m = 0.32_{-0.02}^{+0.02}$, $b = 5.09_{-0.17}^{+0.17}$ when the metallicity estimate is based on I. H. Laseter et al. (2024). We see a similar result when adopting the K. Nakajima et al. (2022) calibration, which results in a best-fit relation of $m = 0.27_{-0.02}^{+0.02}$, $b = 5.48_{-0.17}^{+0.17}$. As was discussed above, those calibrations may overestimate the metallicities at high redshifts. On the other hand, we obtain very similar results when adopting the M. Hirschmann et al. (2023) prescription, with $m = 0.40_{-0.02}^{+0.02}$, $b = 4.36_{-0.17}^{+0.17}$.

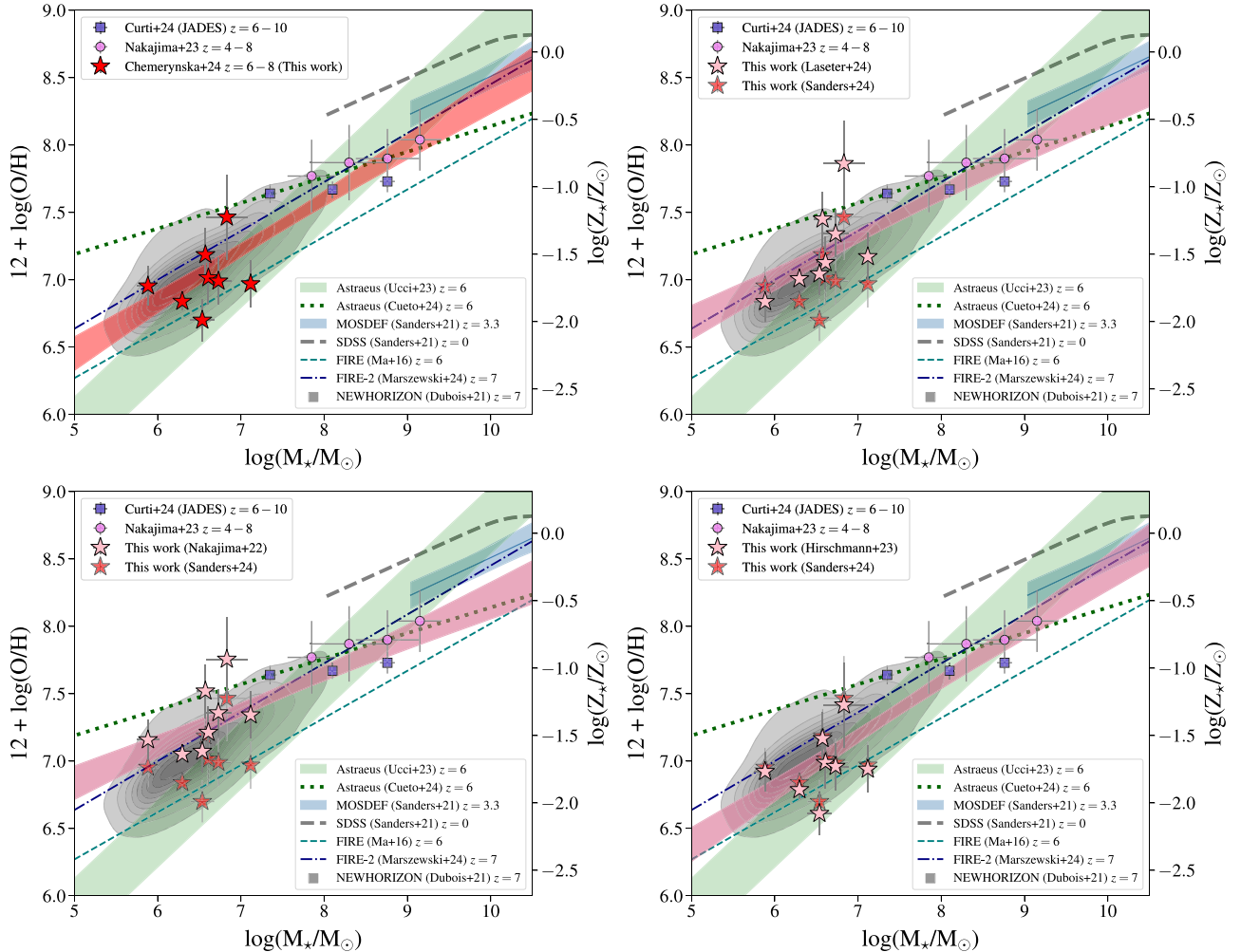

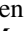
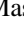
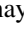


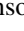







Figure 5. Identical to Figure 1. The MZR at $z = 6-8$ for the lowest-mass galaxies using a single power-law fit. The pink stars represent the metallicities derived by using calibrations from K. Nakajima et al. (2022), I. H. Laseter et al. (2024), and M. Hirschmann et al. (2023; panels from left to right, respectively), along with metallicities derived by the R. L. Sanders et al. (2024; red stars). The fitted MZR is shown in pink.

ORCID iDs

Iryna Chemerynska  <https://orcid.org/0009-0009-9795-6167>
 Hakim Atek  <https://orcid.org/0000-0002-7570-0824>
 Pratika Dayal  <https://orcid.org/0000-0001-8460-1564>
 Lukas J. Furtak  <https://orcid.org/0000-0001-6278-032X>
 Robert Feldmann  <https://orcid.org/0000-0002-1109-1919>
 Jenny E. Greene  <https://orcid.org/0000-0002-5612-3427>
 Michael V. Maseda  <https://orcid.org/0000-0003-0695-4414>
 Themiya Nanayakkara  <https://orcid.org/0000-0003-2804-0648>
 Pascal A. Oesch  <https://orcid.org/0000-0001-5851-6649>
 Seiji Fujimoto  <https://orcid.org/0000-0001-7201-5066>
 Ivo Labbé  <https://orcid.org/0000-0002-2057-5376>
 Rachel Bezanson  <https://orcid.org/0000-0001-5063-8254>
 Gabriel Brammer  <https://orcid.org/0000-0003-2680-005X>
 Sam E. Cutler  <https://orcid.org/0000-0002-7031-2865>
 Joel Leja  <https://orcid.org/0000-0001-6755-1315>
 Richard Pan  <https://orcid.org/0000-0002-9651-5716>
 Sedona H. Price  <https://orcid.org/0000-0002-0108-4176>
 Bingjie Wang  <https://orcid.org/0000-0001-9269-5046>
 John R. Weaver  <https://orcid.org/0000-0003-1614-196X>
 Katherine E. Whitaker  <https://orcid.org/0000-0001-7160-3632>

References

- Atek, H., Furtak, L. J., Oesch, P., et al. 2022, *MNRAS*, 511, 4464
 Atek, H., Labbé, I., Furtak, L. J., et al. 2024, *Natur*, 626, 975
 Atek, H., Richard, J., Kneib, J.-P., & Schaerer, D. 2018, *MNRAS*, 479, 5184
 Baker, W. M., & Maiolino, R. 2023, *MNRAS*, 521, 4173
 Bergamini, P., Acebron, A., Grillo, C., et al. 2023a, *A&A*, 670, A60
 Bergamini, P., Acebron, A., Grillo, C., et al. 2023b, *ApJ*, 952, 84
 Bezanson, R., Labbe, I., Whitaker, K. E., et al. 2024, *ApJ*, 974, 92
 Bian, F., Kewley, L. J., & Dopita, M. A. 2018, *ApJ*, 859, 175
 Bothwell, M. S., Maiolino, R., Kennicutt, R., et al. 2013, *MNRAS*, 433, 1425
 Bouwens, R. J., Illingworth, G., Ellis, R. S., Oesch, P., & Stefanon, M. 2022, *ApJ*, 940, 55
 Bresolin, F., Gieren, W., Kudritzki, R.-P., et al. 2009, *ApJ*, 700, 309
 Brinchmann, J., Charlot, S., White, S. D. M., et al. 2004, *MNRAS*, 351, 1151
 Bruzual, G., & Charlot, S. 2003, *MNRAS*, 344, 1000
 Bunker, A. J., Cameron, A. J., Curtis-Lake, E., et al. 2023, *A&A*, 690, 32
 Carnall, A. C., McLure, R. J., Dunlop, J. S., & Davé, R. 2018, *MNRAS*, 480, 4379
 Carnall, A. C., McLure, R. J., Dunlop, J. S., et al. 2019, *MNRAS*, 490, 417
 Charlot, S., & Fall, S. M. 2000, *ApJ*, 539, 718
 Clarke, L., Shapley, A. E., Sanders, R. L., et al. 2024, arXiv:2406.05178
 Cueto, E. R., Hutter, A., Dayal, P., et al. 2024, *A&A*, 686, A138
 Curti, M., Cresci, G., Mannucci, F., et al. 2017, *MNRAS*, 465, 1384
 Curti, M., D'Eugenio, F., Carniani, S., et al. 2023, *MNRAS*, 518, 425
 Curti, M., Maiolino, R., Curtis-Lake, E., et al. 2024, *A&A*, 684, A75
 Curti, M., Mannucci, F., Cresci, G., & Maiolino, R. 2020, *MNRAS*, 491, 944
 Dayal, P., Hirashita, H., & Ferrara, A. 2010, *MNRAS*, 403, 620
 Dubois, Y., Beckmann, R., Bournaud, F., et al. 2021, *A&A*, 651, A109
 Ellison, S. L., Patton, D. R., Simard, L., & McConnell, A. W. 2008, *ApJL*, 672, L107
 Falcón-Barroso, J., Sánchez-Blázquez, P., Vazdekis, A., et al. 2011, *A&A*, 532, A95
 Ferland, G. J., Chatzikos, M., Guzmán, F., et al. 2017, *RMxAA*, 53, 385
 Finkelstein, S. L., Bagley, M. B., Ferguson, H. C., et al. 2023, *ApJL*, 946, L13
 Fujimoto, S., Arrabal Haro, P., Dickinson, M., et al. 2023, *ApJL*, 949, L25
 Furtak, L. J., Zitrin, A., Plat, A., et al. 2023a, *ApJ*, 952, 142
 Furtak, L. J., Zitrin, A., Weaver, J. R., et al. 2023b, *MNRAS*, 523, 4568
 Garcia, A. M., Torrey, P., Grasha, K., et al. 2024, *MNRAS*, 529, 3342
 Heintz, K. E., Watson, D., Brammer, G., et al. 2023, *Science*, 384, 890–894
 Henry, A., Rafelski, M., Sunnquist, B., et al. 2021, *ApJ*, 919, 143
 Hirschmann, M., Charlot, S., & Somerville, R. S. 2023, *MNRAS*, 526, 3504
 Hunt, L., Dayal, P., Magrini, L., & Ferrara, A. 2016, *MNRAS*, 463, 2002
 Hunt, L., Magrini, L., Galli, D., et al. 2012, *MNRAS*, 427, 906
 Hutter, A., Dayal, P., Yepes, G., et al. 2021, *MNRAS*, 503, 3698
 Izotov, Y. I., Thuan, T. X., & Guseva, N. G. 2021, *MNRAS*, 504, 3996
 Katz, H., Rosdahl, J., Kimm, T., et al. 2023, *OJAp*, 6, 44
 Kewley, L. J., & Ellison, S. L. 2008, *ApJ*, 681, 1183
 Kojima, T., Ouchi, M., Rauch, M., et al. 2020, *ApJ*, 898, 142
 Langeroodi, D., Hjorth, J., Chen, W., et al. 2023, *ApJ*, 957, 39
 Lara-López, M. A., Cepa, J., Bongiovanni, A., et al. 2010, *A&A*, 521, L53
 Laseter, I. H., Barger, A. J., Cowie, L. L., & Taylor, A. J. 2022, *ApJ*, 935, 150
 Laseter, I. H., Maseda, M. V., Curti, M., et al. 2024, *A&A*, 681, A70
 Lee, H., Skillman, E. D., Cannon, J. M., et al. 2006, *ApJ*, 647, 970
 Lian, J. H., Li, J. R., Yan, W., & Kong, X. 2015, *MNRAS*, 446, 1449
 Lilly, S. J., Carollo, C. M., Pipino, A., Renzini, A., & Peng, Y. 2013, *ApJ*, 772, 119
 Ma, X., Hopkins, P. F., Faucher-Giguère, C.-A., et al. 2016, *MNRAS*, 456, 2140
 Ma, X., Hopkins, P. F., Garrison-Kimmel, S., et al. 2018, *MNRAS*, 478, 1694
 Maiolino, R., & Mannucci, F. 2019, *A&ARv*, 27, 3
 Maiolino, R., Nagao, T., Grazian, A., et al. 2008, *A&A*, 488, 463
 Mannucci, F., Cresci, G., Maiolino, R., Marconi, A., & Gnerucci, A. 2010, *MNRAS*, 408, 2115
 Marszewska, A., Sun, G., Faucher-Giguère, C.-A., Hayward, C. C., & Feldmann, R. 2024, *ApJL*, 967, 10
 Mingozi, M., Belfiore, F., Cresci, G., et al. 2020, *A&A*, 636, A42
 Morishita, T., Stiavelli, M., Grillo, C., et al. 2024, *ApJ*, 971, 14
 Nakajima, K., & Ouchi, M. 2014, *MNRAS*, 442, 900
 Nakajima, K., Ouchi, M., Isobe, Y., et al. 2023, *ApJS*, 269, 33
 Nakajima, K., Ouchi, M., Xu, Y., et al. 2022, *ApJS*, 262, 3
 Noeske, K. G., Weiner, B. J., Faber, S. M., et al. 2007, *ApJL*, 660, L43
 Pascale, M., Frye, B. L., Diego, J., et al. 2022, *ApJL*, 938, L6
 Peimbert, M. 1967, *ApJ*, 150, 825
 Pérez-Montero, E., Contini, T., Lamareille, F., et al. 2013, *A&A*, 549, A25
 Pilyugin, L. S., & Grebel, E. K. 2016, *MNRAS*, 457, 3678
 Popesso, P., Concas, A., Cresci, G., et al. 2023, *MNRAS*, 519, 1526
 Price, S. H., Bezanson, R., Labbe, I., et al. 2024, arXiv:2408.03920
 Rinaldi, P., Caputi, K. I., van Mierlo, S. E., et al. 2022, *ApJ*, 930, 128
 Rinaldi, P., Navarro-Carrera, R., Caputi, K. I., et al. 2024, arXiv:2406.13554
 Roberts-Borsani, G., Treu, T., Chen, W., et al. 2023, *Natur*, 618, 480
 Sánchez-Blázquez, P., Peletier, R. F., Jiménez-Vicente, J., et al. 2006, *MNRAS*, 371, 703
 Sanders, R. L., Shapley, A. E., Jones, T., et al. 2021, *ApJ*, 914, 19
 Sanders, R. L., Shapley, A. E., Kriek, M., et al. 2016, *ApJ*, 816, 23
 Sanders, R. L., Shapley, A. E., Reddy, N. A., et al. 2020, *MNRAS*, 491, 1427
 Sanders, R. L., Shapley, A. E., Topping, M. W., Reddy, N. A., & Brammer, G. B. 2024, *ApJ*, 962, 24
 Shapley, A. E., Reddy, N. A., Kriek, M., et al. 2015, *ApJ*, 801, 88
 Somerville, R. S., & Davé, R. 2015, *ARA&A*, 53, 51
 Sparre, M., Hayward, C. C., Springel, V., et al. 2015, *MNRAS*, 447, 3548
 Steidel, C. C., Rudie, G. C., Strom, A. L., et al. 2014, *ApJ*, 795, 165
 Strom, A. L., Steidel, C. C., Rudie, G. C., et al. 2017, *ApJ*, 836, 164
 Torrey, P., Vogelsberger, M., Marinacci, F., et al. 2019, *MNRAS*, 484, 5587
 Tremonti, C. A., Heckman, T. M., Kauffmann, G., et al. 2004, *ApJ*, 613, 898
 Ucci, G., Dayal, P., Hutter, A., et al. 2023, *MNRAS*, 518, 3557
 Vijayan, A. P., Thomas, P. A., Lovell, C. C., et al. 2024, *MNRAS*, 527, 7337
 Wang, B., Leja, J., Bezanson, R., et al. 2023, *ApJL*, 944, L58
 Weaver, J. R., Cutler, S. E., Pan, R., et al. 2023, *ApJS*, 270, 23
 Whitaker, K. E., Franx, M., Leja, J., et al. 2014, *ApJ*, 795, 104
 Zahid, H. J., Dima, G. I., Kudritzki, R.-P., et al. 2014, *ApJ*, 791, 130
 Zitrin, A., Fabris, A., Merten, J., et al. 2015, *ApJ*, 801, 44
 Zou, H., Sui, J., Saintonge, A., et al. 2024, *ApJ*, 961, 173